

Michael Barringer

Karen A. Thole

Department of Mechanical
and Nuclear Engineering,
The Pennsylvania State University,
University Park, PA 16802

Vaidyanathan Krishnan

Corporate Technology,
Chennai, Tamilnadu 600113, India

Evan Landrum

Siemens Energy, Inc.,
Orlando, FL 32817

Manufacturing Influences on Pressure Losses of Channel Fed Holes

Variations from manufacturing can influence the overall pressure drop and subsequent flow rates through supply holes in such applications as film-cooling, transpiration cooling, and impingement cooling that are supplied by microchannels, pipe-flow systems, or secondary air systems. The inability to accurately predict flow rates has profound effects on engine operations. The objective of this study was to investigate the influence of several relevant manufacturing features that might occur for a cooling supply hole being fed by a range of channel configurations. The manufacturing variances included the ratio of the hole diameter to the channel width, the number of channel feeds (segments), the effect of hole overlap with respect to the channel sidewalls, and the channel Reynolds number. The results showed that the friction factors for the typically long channels in this study were independent of the tested inlet and exit hole configurations. The results also showed that the nondimensional pressure loss coefficients for the flow passing through the channel inlet holes and through the channel exit holes were found to be independent of the channel flow Reynolds number over the tested range. The geometric scaling ratio of the hole cross-sectional area to the channel cross-sectional area collapsed the pressure loss coefficients the best for both one and two flow segments for both the channel inlet and channel exit hole. [DOI: 10.1115/1.4025226]

Introduction

Accurately predicting the pressure losses and associated flow rates through supply holes in a variety of gas turbine engine applications such as film-cooling, transpiration cooling, and impingement cooling is essential to prolonging the life of the individual engine hardware components. The coolant flow prediction is critical to ensure that design temperatures of the metal walls are achieved as the walls are exposed to the primary hot gas flow.

The coolant flow rate passing through these internal channels is dependent on the driving pressure difference. As the flow passes through the channel supply inlet holes and exit holes, the flow experiences rapid acceleration, impingement (inlet hole), deceleration, and direction change. As the flow passes through the channel, it experiences frictional losses.

Engine component manufacturing methods, machining tolerances, and part-to-part variations all play a role in setting up the geometric boundary conditions for the flow. For example, the fabrication method for the supply holes and channels may include milling, drilling, and coating operation sequences that result in the flow channels being formed from multiple wall layers. Coolant channels can be formed by machining grooves into one or more of the layered walls. Depending on the manufacturing method, the channel inlet and exit holes can be smaller, equal to, or larger than the channel width and channel height. Depending upon the design, a single inlet hole can deliver flow to one or multiple channels. Likewise, a single exit hole can exhaust coolant flow into the primary gas flow from a single or multiple channel(s). The relative size between the hole diameter, channel width, and channel height all influence the pressure loss experienced by the flow. The number of channel flow segments per inlet hole and exit hole influences pressure loss.

The objectives of the current study were to experimentally measure the pressure losses associated with flow that passes through

different channel and hole geometries that are representative of variations that can occur during engine manufacturing due to construction design methods, machining tolerances, and part-to-part variations. Experimental measurements and computational predictions of pressure losses were conducted for five different design features including *two* geometries that have the hole diameter *less* than the channel width, *one* geometry with the hole diameter *equal* to the channel width, and *two* geometries that have the hole diameter *greater* than the channel width. Each of the five geometries was studied with one and two channels per hole. Another consideration in this study is how the pressure losses were affected for different flow Reynolds numbers.

Relevant Literature

The open literature contains specific examples of estimating the pressure losses for fluid flow through pipes and system components such as elbows, tees, valves, along with pipe entrances and exits. Handbooks on fluid mechanics and hydraulic resistance [1] often report the pressure loss for the various pipe components quantified in terms of nondimensional pressure loss or recovery coefficients, defined as the ratio of the pressure drop across the component to the dynamic pressure of the flow through the component. This method directly correlates the pressure loss to the flow velocity and density at some location upstream of the component, within the component, or downstream of the component.

A variety of pipe-flow system components can be found in the literature and the associated loss coefficient values that are reported are generally average values compiled from multiple pipe component manufacturers. The open literature also reports pressure loss for flow through diffusers, sudden expansions, and sudden contractions usually in graphical form as a function of the ratio of the flow inlet to exit cross-sectional areas, or some other ratio of geometric parameters dominant in the flow field or component [1,2].

Somewhat relevant are the discharge coefficient studies focusing on flow passing through turbine engine film-cooling holes, dilution holes, effusion holes, and impingement holes such as

Contributed by the International Gas Turbine Institute (IGTI) of ASME for publication in the JOURNAL OF TURBOMACHINERY. Manuscript received July 11, 2013; final manuscript received July 15, 2013; published online September 27, 2013. Editor: Ronald Bunker.

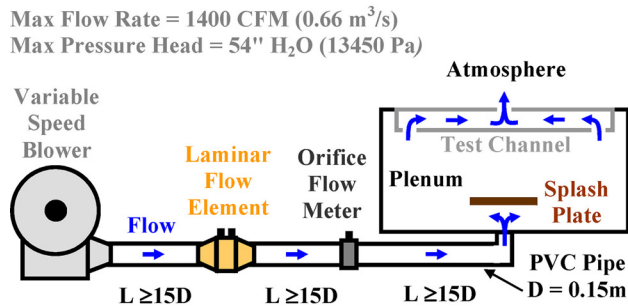


Fig. 1 Schematic of the test stand used to study the internal cooling channels

those performed by numerous researchers, including Hay and Lampard [3], Gritsch et al. [4], and Adkins and Gueroui [5]. These studies report that discharge coefficients are mostly influenced by: (1) the pressure ratio across the holes, (2) the hole geometry including the ratio of the hole length to diameter, entrance and exit radius, orientation with respect to the mainstream flow, and inclination angle, and (3) the cross-flow at the hole entrance and exit.

In general, as the pressure ratio across the hole is increased, the mass flow discharge coefficient increases and then tends to level off as the pressure ratio is further increased to above 1.5 for engine representative conditions. Longer holes, inlet and exit hole edge radiusing, and hole inclination and alignment angles with respect to the cross-flow were all found to influence the mass flow discharge coefficients.

Hay and Lampard [3] state that for sharp-edged holes when the hole length is not sufficient for the flow to fully reattach, the discharge coefficient is limited by the separation of the flow at the hole inlet edges. They also state that for turbine airfoils, the hole length is usually longer so that flow reattachment occurs within the hole, but wall friction losses are negligible compared to the irreversible mixing losses that occur downstream of the separation. Cross-flows tend to modify this flow separation, according to Gritsch et al. [4], who studied discharge coefficients from holes inclined at various angles with and without internal and external cross-flows.

The pressure loss study in Ref. [6] focused on flow through plates containing single and multiple holes with different plate wall thicknesses (t). They found that the pressure loss across the plates correlated well with the dynamic pressure of the flow, along with key geometrical parameters, including the plate wall thickness, hole diameter (D), and the ratio of the open flow area to the cross-sectional duct area. The same study also concluded that as the hole Reynolds number was increased above $Re = 10,000$, the nature and geometry of the flow through the holes were largely insensitive to further increases in the Reynolds number. They also concluded that for thick plates with $t/D > 7.0$, it was more accurate to sum the individual pressure losses for a sudden contraction, a sudden expansion, and a frictional loss.

For the current study, loss coefficients are used to correlate the static pressure loss across the supply holes to the flow dynamic pressure, along with the relationship between the hole and channel geometry. From a general design and manufacturing tolerance perspective, the open literature contains little information on how to best scale the flow pressure losses across holes that supply flow to and from channel geometries that are representative of film cooling, transpiration cooling, and impingement cooling delivery systems. There is also a need for experimental data that reveals how sensitive the pressure loss coefficients are to variations in the size of the holes with respect to the size of the channel, along with a comparison of the experimental data to computational predictions. The computational predictions that are presented in this study complement the experimental data in the sense that the predictions aid the explanation of the pressure loss behavior with

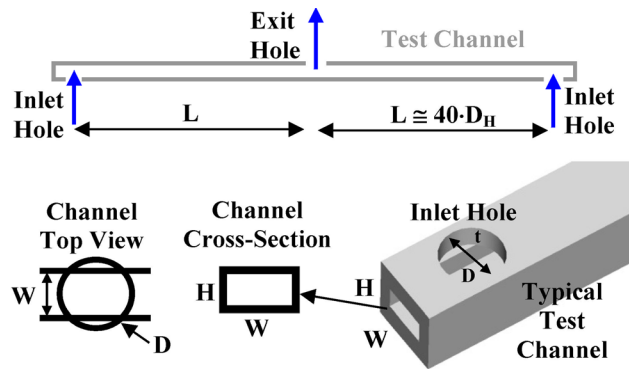


Fig. 2 Schematic of an example cooling channel showing the geometric parameters

respect to the structure of the flow field in and near the holes, including revealing the location of dominant flow turning and illustrating localized regions of flow acceleration, contraction, expansion, circulation, impingement, and deceleration.

Experimental Methodology

A new experimental test stand was designed and constructed to incorporate important geometric features relevant to the inlet and exit holes for channel supplies. The test stand components were designed to minimize uncertainty in measuring the channel pressure. The geometric scaling was also selected such that the target channel Reynolds numbers of $20,000 < Re < 40,000$ were achievable.

Air flow through the internal channels was made possible by the use of a large plenum chamber, as shown in Fig. 1, which was supplied by a variable speed blower. The total mass flow rate was measured using a laminar flow element and an orifice flow meter, both located upstream of the plenum, to improve accuracy over the full range of tested flow rates. All piping was made of polyvinyl chloride. The plenum chamber and test channels were constructed from Lexan polycarbonate to allow for properly sealing the channels. The polycarbonate had a smooth surface finish ($\epsilon = 0$) and, therefore, the channel walls were considered smooth. A baffle (splash) plate was installed at the inlet of the plenum chamber to force the flow to spread out evenly within the plenum. Different test channel configurations were ultimately tested that consisted of both single and multiple inlet and exit holes. The flow passing through the exit hole (or holes) was exhausted directly to laboratory atmospheric conditions.

The test stand was designed such that the walls of the test channels could be interchanged to allow for multiple channel widths and hole diameters, as illustrated in Fig. 2. All inlet and exit holes in the test channels were spaced axially at approximately 40 hydraulic diameters from each other. The primary flow parameters that were of interest in this study included the channel friction factor and the pressure loss coefficient associated with the channel inlet and exit holes. It was not known what effect the inlet and exit holes would have on the overall frictional losses in the channel itself. The channel friction factor was determined by performing a best fit linear regression of the static pressure measurements made along the test channel in the streamwise direction. The velocity is defined using either the mass-averaged velocity passing through the channel or hole and is calculated using the appropriate cross-sectional area of the channel or hole, respectively.

The pressure loss coefficient associated with the holes (K) was defined using the measured static pressure loss ΔP across the hole divided by the dynamic pressure of the flow. All channel and hole velocities in this study were within the incompressible flow regime in which the Mach number was less than 0.26. The pressure loss coefficient was evaluated using the dynamic pressure of the channel flow or by using the dynamic pressure of the flow *within*

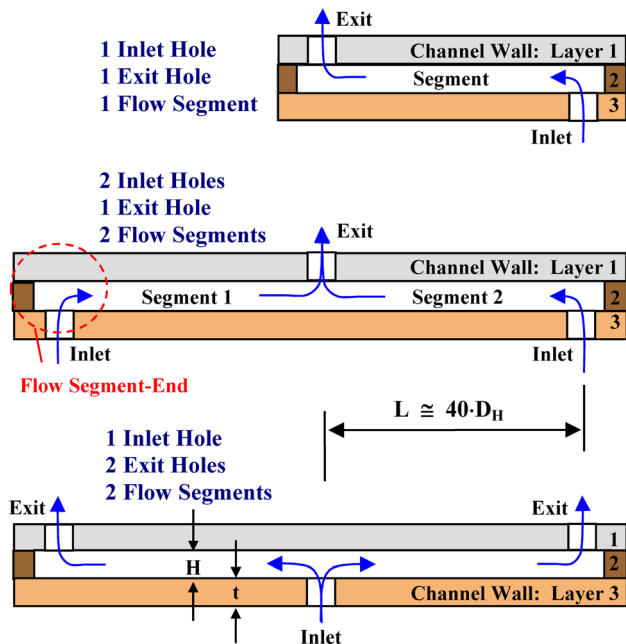


Fig. 3 Schematic cross-sectional views showing the three channel configurations that were tested

the hole. A more in-depth discussion of scaling the hole pressure loss coefficient using local flow conditions is provided in a later section.

Three different channel configurations were investigated in this study, as shown in Fig. 3. The top configuration shown in Fig. 3 included a single inlet hole supplying flow to both a single channel segment and a single exit hole. The middle configuration included two inlet holes supplying flow to two channel segments and only a single exit hole. The bottom configuration included a single inlet hole supplying flow to two channel segments and two exit holes. Each test channel was constructed from three layers of Lexan polycarbonate. Layer 1 was the outermost wall of the channel, Layer 2 was the channel itself (sidewalls), and Layer 3 represented the inner channel wall. Each wall had a thickness equal to the channel height such that $t/H = 1$. Constructing the test channels from multiple layers provided an easy means to test multiple channel widths and hole diameters.

Table 1 includes a summary of the five test channels that were investigated in this study using both a single flow segment and two flow segments. The five test cases include two geometries that have the hole diameter less than the channel width (cases A and B), one geometry that has the hole diameter *nearly equal* to the channel width (case C), and two geometries that have the hole diameter greater than the channel width (cases D and E). Figure 4 shows the inlet and exit holes for both one and two flow segments for case E that has the hole diameter greater than the channel width. Note the difference between the inlet hole and exit hole layering. For the inlet hole (the upper two drawings in Fig. 4), the hole diameter is constant through wall layer 3 and does not interfere with the channel width but does overlap with the channel sidewall layer 2. For the exit hole (the lower two drawings in Fig. 4), the hole diameter is constant through both wall layers 1 and 2, which results in the exit hole intersecting the channel sidewall.

When $D < W$, the shape of the channel sidewall layer near the flow segment-end (see Figs. 3 and 4) was in the form of a half-circle with a radius equal to half of the channel width, as shown in Table 1, such that $2 \cdot r_{\text{channel}} = W$. The center of the half-circle coincided with the center of the hole, such that the two were concentric. When $D > W$, the shape of the channel sidewall layer near the segment-end inlet hole was also a half-circle with a radius equal to half of the channel width; however, the shape of the

sidewall layer near the segment-end exit hole was a circle that matched the hole diameter. The ratio of the hole length to the hole diameter of all holes in this study was between 0.4 and 0.8.

For the entire study, the area ratio of the largest diameter hole tested at the inlet of the test channel to the plenum cross-sectional area was 0.002. This low value of area ratio ensured that the velocity of the air within the plenum resulted in a negligible dynamic pressure and, therefore, the test channel inlet holes were supplied with nearly stagnant air.

Instrumentation and Benchmarking

The plenum chamber was instrumented with two type E thermocouples to measure the air temperature prior to the flow entering the test channel. Four static pressure taps were installed within the plenum chamber walls (one on each sidewall at the midheight of the plenum) in order to measure the pressure within the plenum chamber. Each tap was installed flush with respect to a given wall and was bonded and sealed in place using epoxy. All four plenum pressure measurements agreed with one another to less than 0.8% of the inlet hole dynamic pressure for all tests.

Several static pressure taps were installed along the axial length of the test channel in wall layer 1 (see Fig. 3). The spacing between pressure taps, as shown in Fig. 5, is $0.6D_H$ over the first and last 20% of the channel length L . Twenty percent of the channel length corresponded to approximately $10D_H$. The spacing between pressure taps was chosen to resolve the pressure loss behavior immediately downstream of the inlet hole and immediately upstream of the exit hole. The spacing between pressure taps within the region $0.20 < X/L < 0.80$ was $4.0D_H$, where it was expected to be nearly linear. All pressure taps were installed in the middle of the channel width. For reference, Fig. 5 includes the channel and hole geometry for case B (single flow segment).

Two photographs of the pressure taps installed within wall layer 1 (plenum top wall) are shown in Fig. 6 for the benchmark geometry. It can also be seen that each pressure tap was connected to flexible tubing that was then connected to a 48-channel Scanivalve unit used for data acquisition purposes. All pressure measurements were made using a series of SETRA Model 264 low-differential pressure transducers ranging from 0–25 Pa to as high as 0–12,500 Pa. The laboratory atmospheric pressure was determined using a SETRA Model 370 digital barometer. The factory calibrations for the differential pressure transducers were periodically checked throughout the entire test program using an inclined manometer and digital manometer. Several flow rate calibration tests were also performed using the orifice meter and laminar flow element positioned in series in order to determine their agreement with one another. The agreement was within 1.6% over the full range of flow rates used during the tests. Prior to performing a benchmark test, leak testing was performed by pressurizing the plenum chamber and using soap bubbles.

A benchmark test was performed in order to determine if the measured pressure drop along the channel length was in agreement with friction factor correlations published in the open literature for a fully-developed turbulent flow within a channel. The test channel used for benchmark testing corresponded to case B in Table 1 for one flow segment. In order to establish a single flow segment for the benchmarking, the second flow segment was sealed at the exit hole. The results derived from performing several channel flow tests using the benchmark test geometry are shown in Fig. 7. The measured pressure drop ΔP is plotted from the plenum chamber to the local tap in the channel divided by the plenum pressure. The data points within the region $0.23 < X/L < 0.80$ were used to calculate the channel friction factor. It can be seen in Fig. 7 that within the $0.23 < X/L < 0.80$ region the pressure loss is linear, as expected.

The channel friction factors for the benchmark data in Fig. 7 are given in Fig. 8. The benchmark results are all within 9.2% of the published correlations, which is within the uncertainty bands placed on these correlations [7,8]. Each of the data points in Fig. 8

Table 1 Test matrix of channel and hole geometries (drawings are to scale)

Case	D/W	W/H	A_H/A_C		Inlet hole		Exit hole	
			1 Segment	2 Segments	1 Segment	2 Segments	1 Segment	2 Segments
A	0.61	2.12	0.61	0.31				
B	0.80	1.62	0.81	0.40		Benchmark 	Benchmark 	
C	1.05	1.84	1.59	0.80				
D	1.22	2.12	2.49	1.24				
E	1.60	1.62	3.26	1.63				

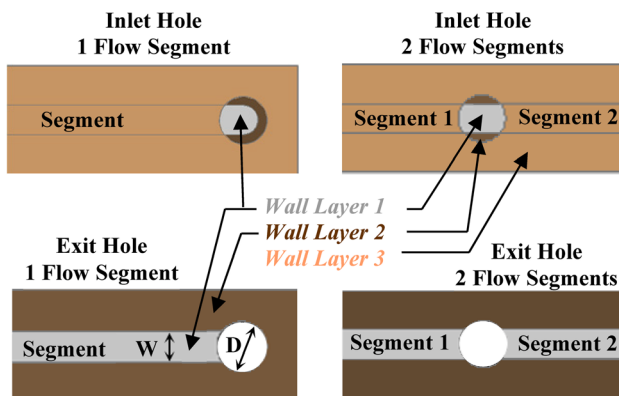


Fig. 4 Plan view drawings (to scale) of the channel inlet and exit holes for example case E

is plotted with its corresponding uncertainty bands. All uncertainty bands were determined using the partial derivative method of Kline and McClintock [9]. The experimental uncertainty in the channel friction factor is 6.1% at $Re = 20,600$ and 4.7% at $Re = 39,400$.

The loss coefficients for the benchmark inlet hole were calculated using the mass-averaged velocity passing through the hole, the air density within the plenum chamber, and the pressure drop from the plenum chamber to the channel axial location where the

pressure loss began its linear behavior (channel taps nos. 14–17 or $X/L = 0.23$), as shown in Fig. 7.

Comparisons of the loss coefficients were made using a subset of the pressure taps in this same location; however, to within the uncertainty of the measurements, there were no differences noted in the reported values. The loss coefficient for the exit hole was evaluated using the static pressure drop from the channel axial location where the pressure loss ended its linear behavior (channel taps nos. 33–36, or $X/L = 0.91$), as shown in Fig. 7, to the laboratory ambient pressure. The calculated value of K for the exit hole also did not change significantly if selecting a subset of the pressure taps in this same location.

The experimental uncertainty in the pressure loss coefficient for the inlet hole is 6.9% at $Re = 20,600$ and 4.5% at $Re = 39,400$. The experimental uncertainty in the pressure loss coefficient for the exit hole is 9.5% at $Re = 20,600$ and 6.5% at $Re = 39,400$. It can be seen in Fig. 9 that the loss coefficient was found to be independent of the channel Reynolds number to within experimental uncertainty. These results are similar to loss coefficients for minor head losses given by the literature [7,10] for flow through bends, tees, and elbows.

Computational Methodology

The pressure loss coefficients and channel friction factors were also predicted using the commercial computational fluid dynamics (CFD) software FLUENT [11]. The simulations were performed using a second-order discretization of all variables within the 3D

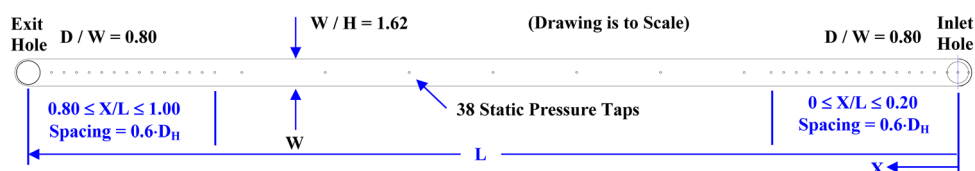


Fig. 5 Static pressure tap locations in wall layer 1 for a single flow segment (Case B)

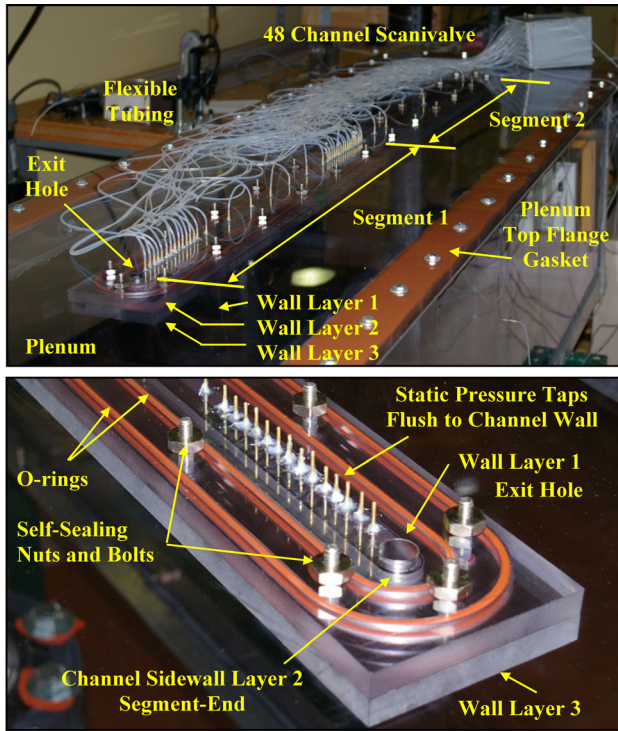


Fig. 6 Photos showing the static pressure taps installed in the primary wall (plenum top wall) for the benchmark test channel

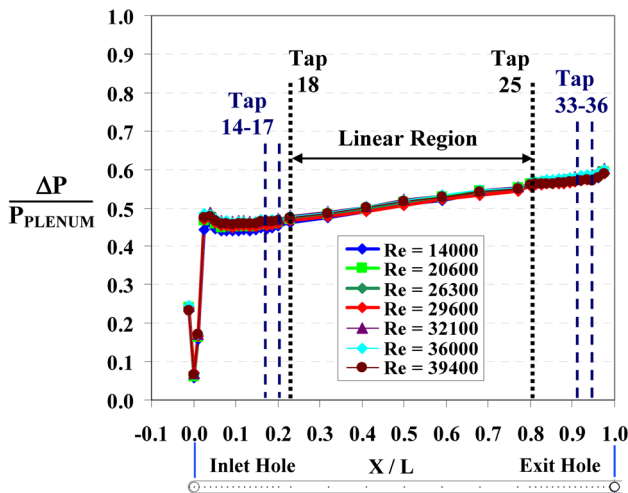


Fig. 7 Graph of the measured pressure drop from the plenum to the local channel tap for the benchmark geometry at several Reynolds numbers

pressure-based formulation of the steady Navier–Stokes equations, a two equation turbulence model, and the energy equation. The air flow was simulated as an ideal gas using the two-equation realizable $k-\epsilon$ turbulence model with enhanced wall functions. The internal cooling channels were modeled using a large plenum chamber that supplied flow to the inlet hole(s).

For each simulation, the inlet plenum was at a volume that was $10D \times 10D \times 10D$. A much larger plenum chamber was used for the exit hole(s), which was $15D$ long \times $15D$ wide, having a height between $60-240D$ in order to allow the exit hole jet flow to slow to near zero velocity. An example mesh used for the benchmark geometry is shown in Fig. 10.

The boundary conditions used to perform each simulation corresponded to the experimental test conditions for a given channel

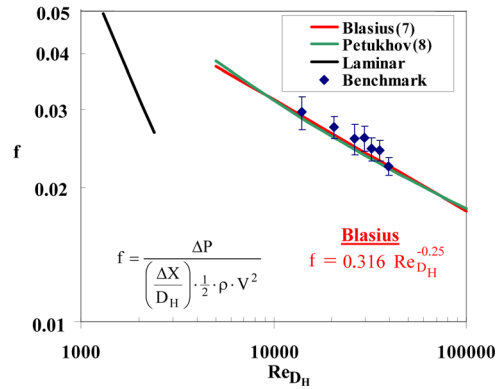


Fig. 8 Channel friction factors for the benchmark test (case B, 1 segment)

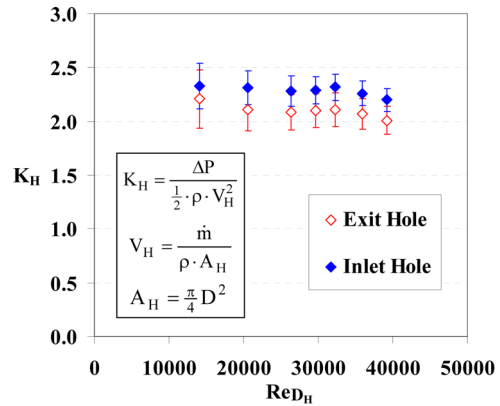


Fig. 9 Pressure loss coefficients for the channel inlet and exit holes versus the channel Reynolds number (case B, 1 segment)

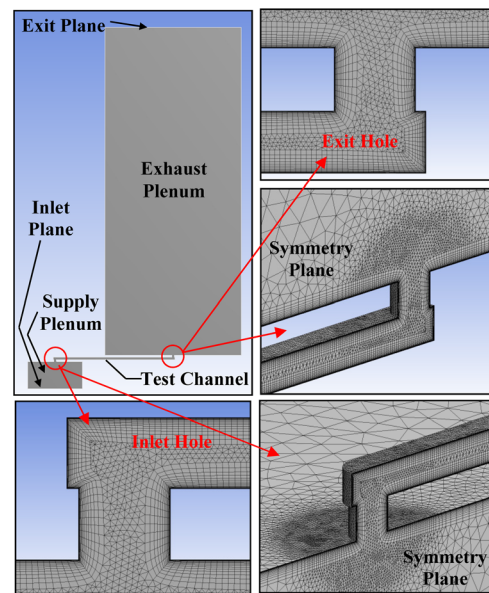


Fig. 10 Example computational domain and mesh used for Case B with 1 flow segment

geometry. The inlet plane to the supply plenum was set as a mass-flow inlet boundary, while the exit plane of the exhaust plenum was set as an outlet boundary condition. A symmetry boundary condition was also used.

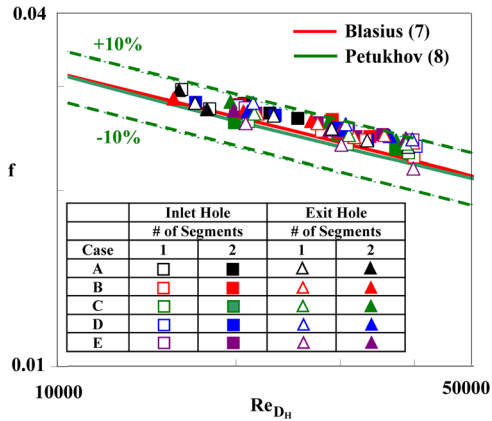


Fig. 11 Plot of the channel friction factor for all test channel geometries in Table 1

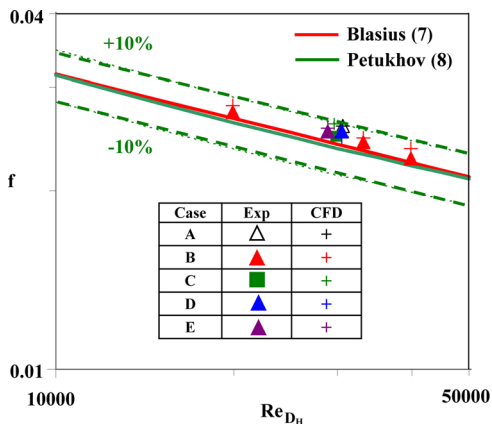


Fig. 12 Comparisons of the channel friction factor between the experiments and CFD predictions

Convergence was considered established for a given simulation once all residuals had reached 10^{-4} and the mass continuity between the supply and exhaust plenum(s) matched to within 0.5%. Typically, this required 1000 to 1500 iterations. A grid independence study was also performed using an initial mesh of 0.37×10^6 cells and refining it three times, including grids containing a total of 0.91, 1.67, and 2.50×10^6 cells. The refinements focused on increasing the cell density in regions of high velocity gradients near and within the inlet and exit hole(s) and along the walls of the channel. The difference in the friction factor from the initial grid of 0.37×10^6 cells to the refined grid of 2.50×10^6 cells was 1.24%, 0.86%, and 0.02%, respectively. The difference in the loss coefficient from the initial to the refined grid was less than 1.0%. A typical mesh, once refined contained, nearly 2.0 million cells.

Channel Friction Factors

For each test that was performed, the channel frictional losses were compared with published correlations in terms of a friction factor. Similar to the benchmark test, the friction factor for all test case geometries was found to be within 10% of the Blasius [7] and Petukhov [8] correlations. In Fig. 11, it can be seen that the inlet and exit hole configurations did not significantly affect the calculated friction factors.

The computational predictions of the channel friction factor are displayed in Fig. 12 for all five geometry cases. Computations were first performed for case B and the agreement between the experimental data and the predictions was found to be within 8.3% over the full range of channel Reynolds numbers. Subsequent

predictions for the other four geometry cases were performed at the middle of the channel flow range near $Re = 30,000$. It can be seen there was agreement between the experimental data, the predicted values, and the correlations.

Inlet and Exit Hole Losses

The inlet and exit hole pressure loss coefficients K for all test case geometries were found to be nearly independent (within experimental uncertainty) of the channel flow Reynolds number in the range of $20,000 < Re < 40,000$, which is in agreement with the conclusions from published literature [6,7]. The computations also predicted this independent relationship; therefore, the focus of the data analysis was shifted to different geometric and velocity scaling parameters in order to determine which best correlated the hole pressure loss. Averages of the loss coefficients across the entire Reynolds number range were used for these analyses.

Inlet Hole Losses. The open literature definition of the loss coefficient typically uses the static pressure loss across the hole relative to the dynamic pressure of the flow within the hole. This definition, however, may not be relevant to all of the cases investigated in this present study. Other definitions were investigated, such as the static pressure drop across the hole relative to the dynamic pressure of the flow within the channel. The dynamic pressure of the flow within the channel is defined using the mass-averaged velocity within the channel, which is based on the cross-sectional area of the channel.

The loss coefficient for the inlet hole was measured for all cases given in Table 1, as indicated in Fig. 13. The loss coefficient for the inlet hole is defined using the pressure loss from the plenum chamber to the channel region $X/L = 0.10-0.15$, which corresponded to the axial location in which the channel static pressure begins a linear loss behavior. In Figs. 13(a) and 13(b), the loss coefficients are defined using the dynamic pressure of the flow within the inlet hole. In Figs. 13(c) and 13(d), the loss coefficients are defined using the dynamic pressure of the flow within the channel. The computational predictions corresponding to each test case in Table 1 for the inlet hole are also included in Fig. 13. The predictions are in fairly good agreement with the experimental data for most of the geometries and show consistent trends of the pressure loss coefficient.

Within Fig. 13, two geometric scaling ratios were considered, including the ratio of the hole cross-sectional area to the channel cross-sectional area A_H/A_C and the ratio of the hole diameter to the channel width D/W . In Fig. 13(a), when $A_H/A_C < 1$, the loss coefficient data fall within the relatively small range from $1.3 < K_H < 2.5$, but dramatically increases when $A_H/A_C > 1$. This same behavior is seen when the inlet hole loss coefficient is plotted versus the ratio D/W in Fig. 13(b). When $D/W < 1$, the inlet hole does not overlap the channel sidewalls and the loss coefficient is relatively low and within a small range when using the hole dynamic pressure. As the ratio of D/W is increased above unity, the inlet hole overlaps the channel sidewalls and the loss coefficient then increases when using the hole dynamic pressure. The geometric scaling ratio of A_H/A_C , however, collapses the data for both the one- and two-flow segments significantly better than D/W . This result has important implications since it provides a means of knowing the loss coefficients for additional flow segments per inlet hole.

For the same physical pressure drop across the inlet hole, Figs. 13(c) and 13(d) show an opposite trend than Figs. 13(a) and 13(b), when using the dynamic pressure of the flow within the channel. In Fig. 13(c), when $A_H/A_C > 1$, the loss coefficient data fall within the relatively small range from $1.5 < K_C < 1.8$, but dramatically increases when A_H/A_C is reduced to below $A_H/A_C < 1$. This same behavior is seen when the inlet hole loss coefficient is plotted versus the ratio D/W in Fig. 13(d). When $D/W > 1$, the inlet hole overlaps the channel sidewalls and the loss coefficient is relatively low and within a small range when using the channel

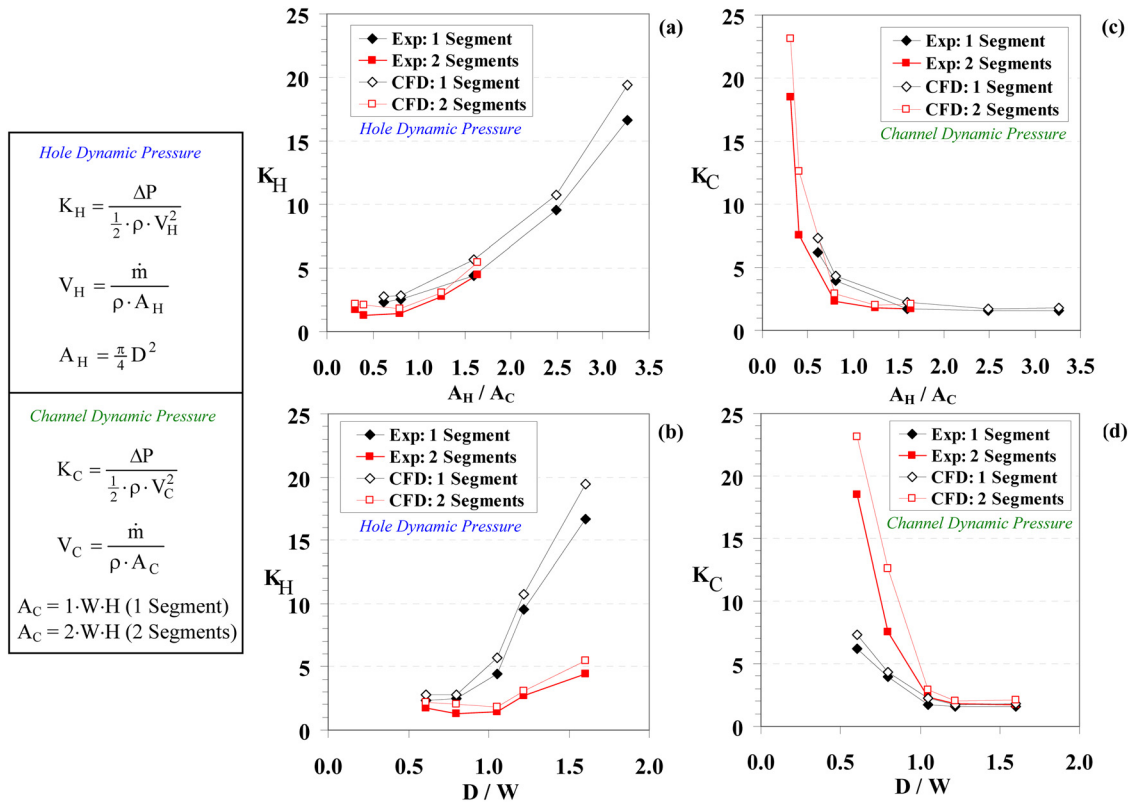


Fig. 13 Inlet hole loss coefficients for various scaling parameters (cases A–E)

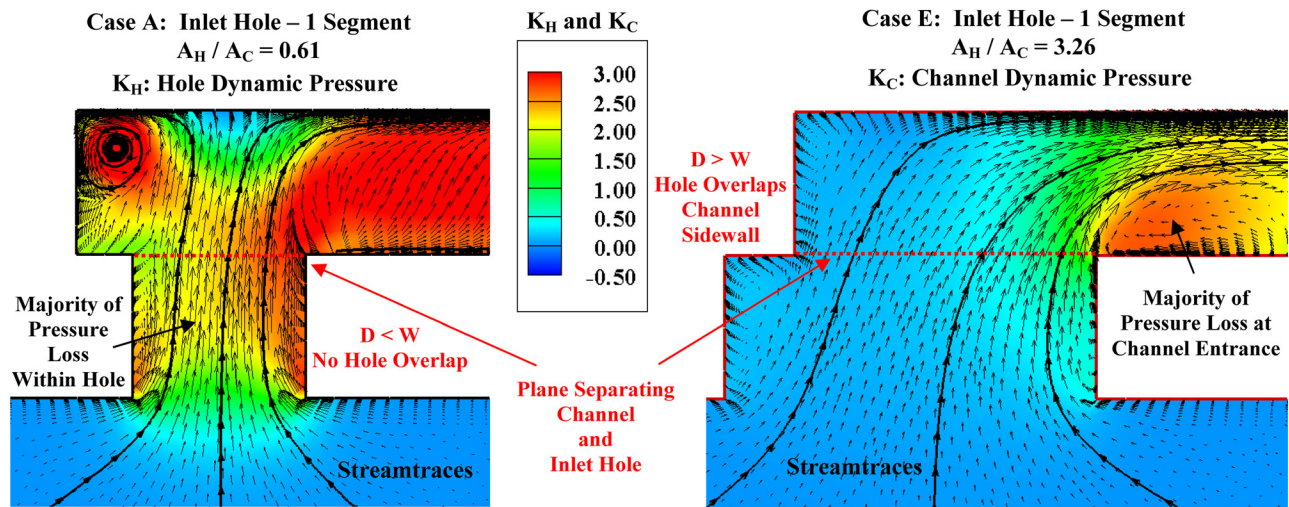


Fig. 14 The CFD contours of loss coefficient K within the symmetry plane for the inlet hole showing that the loss is dominant within the hole for case A versus within the channel for case E ($Re_{D_H} = 30,000$)

dynamic pressure. Figures 13(c) and 13(d) also show that the geometric scaling parameter A_H/A_C is better at collapsing the data from both one and two flow segments than the ratio D/W .

When $A_H/A_C < 1$, the hole cross-sectional area is the minimum area through which the flow passes and, therefore, the hole is the primary flow restriction with the maximum flow velocity. Conversely, when $A_H/A_C > 1$ the channel cross-sectional area is the minimum area through which the flow passes and, therefore, the channel is the primary flow restriction with the maximum flow velocity. This can be seen in the flowfield predictions shown in Fig. 14, within the computation symmetry plane (see Fig. 10), for the inlet hole supplying flow to one segment for case A, in which

$A_H/A_C < 1$ and case E, in which $A_H/A_C > 1$. Contour levels of pressure loss coefficients K_H and K_C are included in Fig. 14 along with velocity vectors that are normalized to the mass-averaged channel velocity at $X/L = 0.50$. The channel Reynolds number for each flowfield prediction in Fig. 14 is approximately $Re = 30,000$.

It can be seen in Fig. 14 that the majority of the pressure loss for case A is predicted within the hole where the velocity vectors are at a maximum inside a *vena contracta* that is highlighted using stream traces. This is consistent with statements noted earlier from Hay and Lampard [3] regarding cooling holes typically experiencing flow separation within the hole due to the short hole length and high pressure ratio. For case A, as the flow passes

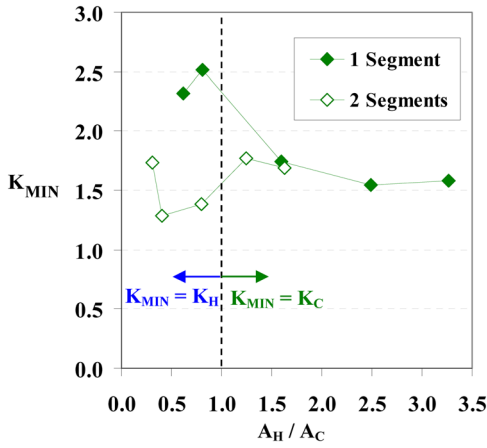


Fig. 15 Inlet hole loss coefficients using K_{min}

through the exit plane of the inlet hole, the pressure loss is, on average, near $K_H = 2.5$, compared to $K_H = 2.8$ just downstream of the channel entrance.

For case E in Fig. 14 the majority of the pressure loss is predicted downstream of the hole in the channel entrance region where the velocity vectors are also at a maximum and located above a large separation region along the channel wall. At the point that the flow passes through the exit plane of the inlet hole for case E, the pressure loss is low, on average, near $K_C = 0.5$; however, at the point that the flow sharply turns into the channel inlet plane the loss is near $K_C = 1.5$, compared to $K_C = 1.8$ within the channel.

Additional loss mechanisms can also be seen in Fig. 14. For example, in case A the flow is predicted to impinge on the channel upper wall and then spread in all directions and in the upper left

corner of the segment-end the flow is predicted to have a recirculation vortex. For case E, there is a small flow separation along the right-hand side wall of the inlet hole and very small recirculation in the left-hand side hole and channel corners.

The loss coefficient for the inlet hole can also be defined using the minimum cross-sectional area by using the dynamic pressure within the hole when $A_H/A_C < 1$ and the dynamic pressure within the channel when $A_H/A_C > 1$. This definition of the loss coefficient results in the range of $1.3 < K_{min} < 2.5$ for all of the inlet hole geometries tested in this study. In Fig. 15, K_{min} is plotted versus the scaling parameter A_H/A_C . It can be seen why this scaling method was chosen as the best to collapse the data from the inlet hole since it results in a convenient small range of the loss coefficient. When $A_H/A_C < 1$ in Fig. 15, a difference in the trend of K_{min} was observed for one versus two flow segments. This difference was attributed to the additional loss mechanisms that were predicted to be present near the channel segment-end for one flow segment that would not be present for two flow segments when $A_H/A_C < 1$; including, for example, the recirculation vortex shown in Fig. 14.

Overall, the data and computations showed that the inlet hole pressure loss collapses and scales best to the flow dynamic pressure at the location where the flow experiences maximum velocity. This corresponds to the hole dynamic pressure when $A_H/A_C < 1.0$ and to the channel dynamic pressure when $A_H/A_C > 1.0$.

Exit Hole Losses. The pressure loss coefficient for the exit hole was also measured for all cases given in Table 1, as indicated in Fig. 16. The loss coefficient for the exit hole is defined using the static pressure loss from the channel region $X/L = 0.90-0.95$ to the laboratory ambient pressure. The channel region $X/L = 0.90-0.95$ corresponds to the axial location in which the channel static pressure ends its nearly linear loss behavior.

In Figs. 16(a) and 16(b), the loss coefficients are plotted using the dynamic pressure of the flow within the exit hole. In Figs. 16(c) and 16(d), the loss coefficients are plotted using the

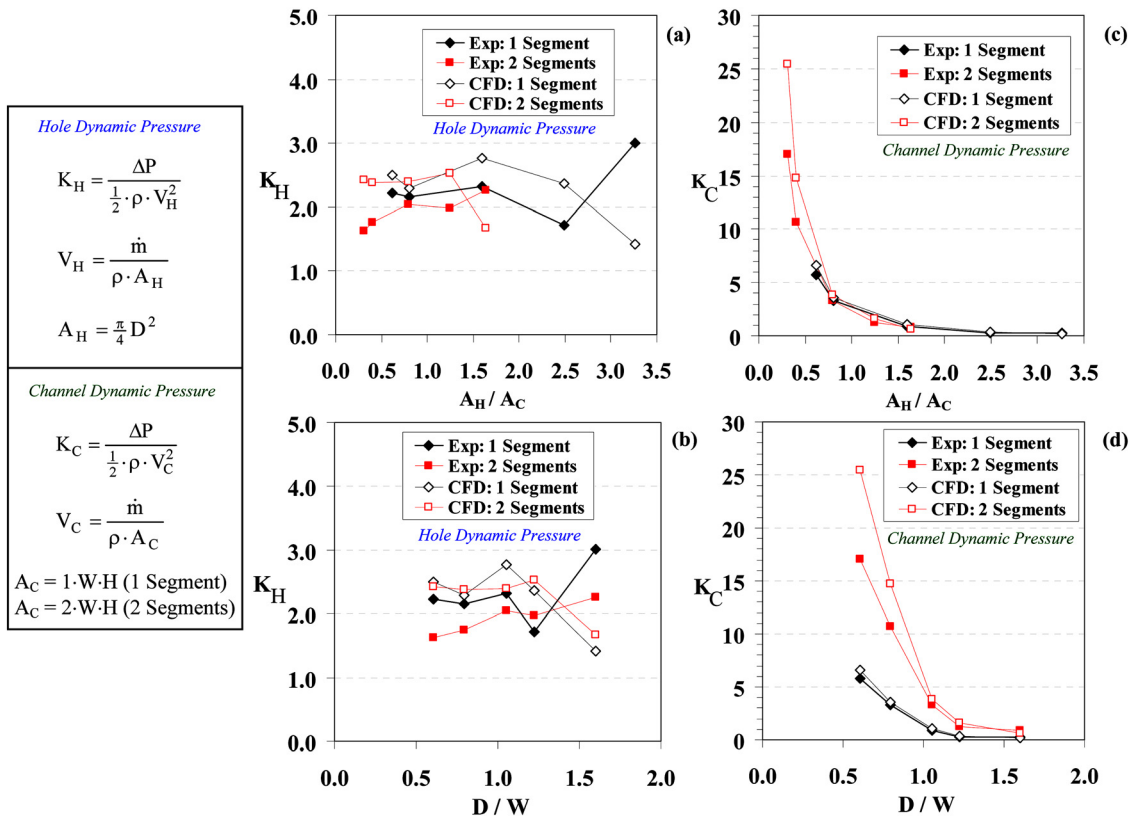


Fig. 16 Exit hole loss coefficients for various scaling parameters (cases A-E)

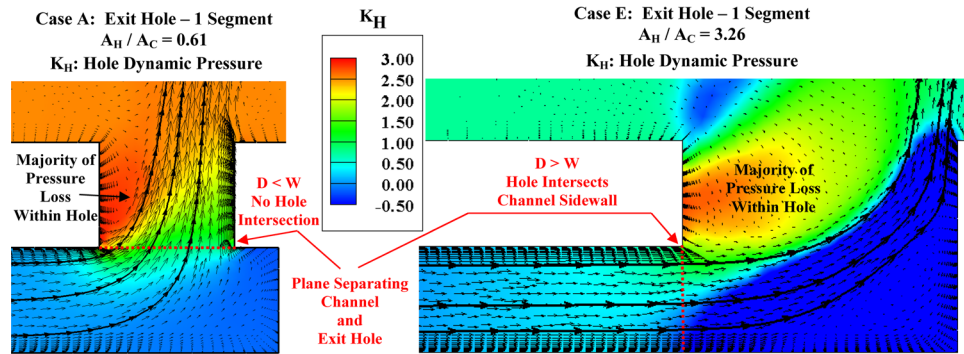


Fig. 17 The CFD contours of loss coefficient K within the symmetry plane for the exit hole showing that the loss is dominant within the hole for both cases A and E ($Re_{D_H} = 30,000$)

dynamic pressure of the flow within the channel. The computational predictions corresponding to each test case in Table 1 for the exit hole are also included in Fig. 16. The predictions are in fairly good agreement with the experimental data for most of the exit hole geometries and show consistent trends of the pressure loss coefficient.

Within Fig. 16, the same two geometric scaling ratios A_H/A_C and D/W are used for the exit hole as were used for the inlet hole. In Fig. 16(a), it can be seen that the loss coefficients for the exit hole fall within a relatively small range from $1.6 < K_H < 3.0$ over the entire range of A_H/A_C for both the one- and two-flow segments, when defined using the dynamic pressure of the flow within the hole. This same behavior is seen when the exit hole loss coefficient is plotted versus D/W in Fig. 16(b). As with the inlet hole, Figs. 16(c) and 16(d) show a different trend than Figs. 16(a) and 16(b) for the same physical pressure drop across the exit hole.

The relatively small range of K_H within Figs. 16(a) and 16(b) suggests that the hole dynamic pressure is a better scaling parameter for the exit hole than the channel dynamic pressure. Computational predictions of the flowfield within and near the exit hole for cases A and E for a single flow segment are shown in Fig. 17 using the dynamic pressure of the flow within the hole. Figure 17 clearly shows that the pressure loss for the exit hole is most prevalent within the hole for both case A and case E. Figure 17 also shows some additional predicted loss mechanisms, including flow separation along the left-hand side wall of the exit hole for both case A and case E, ingestion into the hole from the ambient room for case E, and a small recirculation in the hole lower right corner for case E.

It can be seen in Fig. 17 that the channel flow is predicted to make a sharp 90 deg bend prior to the flow accelerating and entering the hole for case A. The flow for case A then continues to accelerate within the hole and must then rapidly expand as the static pressure equilibrates with the ambient room at the hole exit plane. The same bend in the flow is also predicted for case E but the bend is predicted to be *within the hole*, due to the fact that the hole intersects the channel sidewalls for case E when $D > W$ but does not intersect the channel sidewalls for case A when $D < W$. For case E, the channel flow enters the hole without bending or contracting but instead must immediately expand inside the hole, thereby slowing down into the larger cross-sectional region of the hole. This diffusion process is evident from the slightly negative loss coefficient values within and near the lower right of the hole since the static pressure has increased. Once inside the hole for case E, the flow *then* makes a 90 deg bend to exhaust to the ambient room by which the static pressure equilibrates to the ambient room pressure at the hole exit plane.

The rapid expansion of the flow in and near the hole exit plane in which the flow static pressure must equilibrate with the ambient room pressure results in most of the pressure loss occurring within the hole for all exit holes studied. This is in contrast to the inlet

hole flow behavior in which most of the pressure loss occurred at the location of the maximum flow field velocities.

Conclusions

Experimental and computational studies were conducted to determine the friction factor and pressure loss coefficients associated with flow that passes through different channel and hole geometries that are representative of variations that can occur during engine manufacturing. These variations can exist due to construction design methods, dimensional tolerances, and part-to-part variations. For example, the supply holes and channel fabrication method may include milling, drilling, and coating operations that result in the layered wall scenarios similar to those included in this investigation. A total of five geometric scenarios were presented that included two geometries with the hole diameter less than the channel width, one geometry with the hole diameter equal to the channel width, and two geometries with the hole diameter greater than the channel width. The test geometries included one and two flow segments per inlet and exit hole(s), for a combined total of twenty test cases.

All measured and predicted channel friction factor results were within 10% of published literature correlations for fully-developed turbulent channel flow. The inlet and exit hole geometry of the test channel did not significantly affect the calculated values for the channel friction factor. The inlet and exit hole pressure loss coefficients were found to be independent of the channel Reynolds numbers tested in this study.

The geometric scaling ratio of the hole cross-sectional area to the channel cross-sectional area collapsed the loss coefficients the best for both one- and two-flow segments for both the inlet and exit hole. This is important because it allows the results of this study to be applied to additional flow segments per hole.

Overall, the data and computations showed that the inlet hole pressure loss collapses and scales best to the flow dynamic pressure at the location where the flow experiences maximum velocity. This corresponds to the hole dynamic pressure when $A_H/A_C < 1.0$ and to the channel dynamic pressure when $A_H/A_C > 1.0$. The data and computations also showed that the exit hole pressure loss scales best to the hole dynamic pressure for all A_H/A_C considered in this study. The rapid expansion of the flow in and near the exit hole exit plane in which the flow static pressure must rapidly equilibrate with the ambient room pressure results in most of the pressure loss occurring within the exit hole.

Acknowledgment

The authors would like to thank Siemens Energy, Inc. for sponsoring this research work.

Nomenclature

A = area (cross-sectional)
 D = diameter of hole

D_H = hydraulic diameter, $D_H = 4 \cdot W \cdot H / (2 \cdot W + 2 \cdot H)$
 f = friction factor, $f = \Delta P / ((\Delta X / D_H)(1/2) \cdot \rho \cdot V^2)$
 H = height of channel
 K = loss coefficient, $K = \Delta P_S / ((1/2)\rho \cdot V^2)$
 L = channel length between holes
 \dot{m} = mass flow rate
 P = pressure
 r = radius
 R = gas constant
 Re = Reynolds number, $Re_{D_H} = \rho \cdot V \cdot D_H / \mu$
 t = wall thickness
 T = temperature
 V = velocity (mass-averaged), $V = \dot{m} / (\rho \cdot A)$
 W = width of channel
 X = distance in streamwise direction

Greek Symbols

Δ = change in variable
 ε = equivalent wall surface roughness
 μ = dynamic viscosity
 ρ = density, $\rho = P_S / (R \cdot T_S)$

Subscripts

C = channel

H = hole
 \min = minimum
 S = static conditions

References

- [1] Idel'chik, I. E., 1994, *Handbook of Hydraulic Resistance*, 3rd ed., CRC, Boca Raton, FL.
- [2] Miller, D. S., 1978, *Internal Flow Systems*, BHRA Fluid Engineering, Cranfield, UK.
- [3] Hay, N., and Lampard, D., 1998, "Discharge Coefficient of Turbine Cooling Holes: A Review," *ASME J. Turbomach.*, **210**, pp 314–319.
- [4] Gritsch, M., Schulz, A., and Wittig, S., 2001, "Effect of Crossflows on the Discharge Coefficient of Film Cooling Holes With Varying Angles of Inclination and Orientation," *ASME J. Turbomach.*, **V123**, pp. 781–787.
- [5] Adkins, R. C., and Gueroui, D., 1986, "An Improved Method for Accurate Prediction of Mass Flow Through Combustion Liner Holes," *ASME J. Eng. Gas Turbines Power*, **108**, pp. 491–497.
- [6] Engineering Sciences Data Unit 81039, 1981, "Pressure Losses Across Orifice Plates, Perforated Plates and Thick Orifice Plates in Ducts," Internal Flow Panel, Engineering Sciences Data Unit Ltd., Specialised Printing Services Ltd., London.
- [7] Munson, B., Young, D., and Okishi, T., 1998, *Fundamentals of Fluid Mechanics*, 3rd ed., John Wiley and Sons, Hoboken, NJ.
- [8] Petukhov, B. S., 1970, *Advances in Heat Transfer*, Vol. 6, T. F. Irvine and J. P. Hartnett, eds., Academic, New York.
- [9] Kline, S. J., and McClintock, F. A., 1953, "Describing Uncertainties in Single-Sample Experiments," *ASME Mechanical Eng.*, **75**, pp. 3–8.
- [10] White, F. M., 1979, *Fluid Mechanics*, McGraw-Hill, New York.
- [11] Ansys, 2009, "ANSYS FLUENT (version 12.0.16)," Ansys Inc., Canonsburg, PA.